

Postprint

This document is the Accepted Manuscript version of a Published Work that appeared in final form in
after peer review and technical editing by the publisher.

To access the final edited and published work see:

Access to the published version may require subscription.

When citing this work, please cite the original published paper.

Large magnetic exchange coupling in rhombus-shaped nanographenes with zigzag periphery

Shantanu Mishra¹, Xuelin Yao², Qiang Chen², Kristjan Eimre¹, Oliver Gröning¹,
Ricardo Ortiz^{3,4}, Marco Di Giovannantonio¹, Juan Carlos Sancho-García⁴,
Joaquín Fernández-Rossier⁵, Carlo A. Pignedoli¹, Klaus Müllen², Pascal Ruffieux¹,
Akimitsu Narita^{2,6*}, Roman Fasel^{1,7*}

¹nanotech@surfaces Laboratory, Empa—Swiss Federal Laboratories for Materials Science and Technology, Dübendorf, Switzerland

²Department of Synthetic Chemistry, Max Planck Institute for Polymer Research, Mainz, Germany

³Department of Applied Physics, University of Alicante, Sant Vicent del Raspeig, Spain

⁴Department of Chemical Physics, University of Alicante, Sant Vicent del Raspeig, Spain

⁵QuantaLab, International Iberian Nanotechnology Laboratory, Braga, Portugal

⁶Organic and Carbon Nanomaterials Unit, Okinawa Institute of Science and Technology Graduate University, Okinawa, Japan

⁷Department of Chemistry and Biochemistry, University of Bern, Bern, Switzerland

*Corresponding authors: narita@mpip-mainz.mpg.de and roman.fasel@empa.ch

Nanographenes with zigzag edges are predicted to manifest non-trivial π -magnetism resulting from the interplay of concurring electronic effects, such as hybridization of localized frontier states and Coulomb repulsion between valence electrons. This provides a chemically tunable platform to explore quantum magnetism at the nanoscale and opens avenues toward organic spintronics. The magnetic stability in nanographenes is thus far limited by the weak magnetic exchange coupling, which remains below the room temperature thermal energy. Here, we report the synthesis of large rhombus-shaped nanographenes with zigzag periphery on gold and copper surfaces. Single-molecule scanning probe measurements show an emergent magnetic spin singlet ground state with increasing nanographene size. The magnetic exchange coupling in the largest nanographene ($C_{70}H_{22}$, containing five benzenoid rings along each edge), determined by inelastic electron tunneling spectroscopy, exceeds 100 meV or 1160 K, which outclasses most inorganic nanomaterials and survives on a metal electrode.

Magnetism in solids is usually associated to *d*- or *f*-block elements. However, since the isolation of graphene, the field of carbon magnetism has gained increased traction¹. Though

ideal graphene is a diamagnetic semimetal, many of its derivative nanostructures (nanographenes) are predicted to manifest magnetism that is distinct from magnetism in molecules and solids containing transition metal atoms. First, in contrast to the localized nature of magnetic moments in transition metal atoms, unpaired electrons in nanographenes are hosted by molecular π -orbitals, which extend over several carbon atoms. Second, the emergence of magnetic moments in nanographenes, among other theoretical interpretations²⁻⁵, can be understood from two competing phenomena relevant in the context of the current research: (1) hybridization energy, which is responsible for the formation of the highest occupied and lowest unoccupied molecular orbitals (HOMO and LUMO), leading to a non-magnetic (closed-shell) ground state, and (2) electrostatic Coulomb repulsion between valence electrons, which promotes the formation of singly occupied molecular orbitals (SOMOs) hosting unpaired spins, resulting in a magnetic (open-shell) ground state. These two energy scales, along with the magnetic ordering between unpaired spins, can be efficiently tailored through a rational design of the shape, size and edge structure of nanographenes. It has long been known that hybridization energy may be strongly reduced or even completely removed in nanographenes with zigzag edges⁶⁻⁸, with higher anthrenes⁹⁻¹¹ and zethrenes¹²⁻¹⁴ being typical examples of nanographenes with open-shell characters. In recent years, this concept has also been utilized to fabricate open-shell nanographenes on surfaces, whose magnetic ground states have been directly evidenced with the scanning tunneling microscope (STM) through detection of Kondo interactions between localized spins and conduction electrons of metal surfaces, and spin excitations of coupled spin systems¹⁵⁻¹⁹.

Experimental realization of nanographenes containing zigzag edges is largely restricted to structures with a mixture of zigzag and armchair edges, with prominent examples being anthrenes, zethrenes and periacenes²⁰⁻²², and synthesis of nanographenes with all sides consisting of zigzag edges (zigzag nanographenes, ZNGs) has proven challenging. Triangular ZNGs²³, which exist as neutral radicals^{24,25}, have been recently synthesized on metal and insulator surfaces under ultrahigh vacuum²⁶⁻²⁸. However, evidence of magnetism in these nanographenes is indirect, and relies on the detection of the probability densities attributed to the SOMOs and the associated unoccupied molecular orbitals (SUMOs) by scanning tunneling spectroscopy (STS). On the other hand, solution synthesis of large ZNGs is limited to closed-shell systems²⁹⁻³². Here, we report the on-surface synthesis of rhombus-shaped ZNGs, hereafter $[n]$ -rhombenes, where n is the number of benzenoid rings along an edge, with $n = 4$ ($C_{48}H_{18}$, **1**) and 5 ($C_{70}H_{22}$, **2**), which represent the largest ZNGs synthesized to date (Fig. 1). Our inelastic electron tunneling spectroscopy (IETS) measurements, supported by theoretical models, show that $[n]$ -rhombenes acquire an open-shell ground state with increasing size. The magnetic exchange coupling (MEC) in the larger nanographene, **2**, is directly determined to be 102 meV, which exceeds the room temperature thermal energy by a factor of four, and surpasses the MEC in most known transition metal nanomagnets³³.

Results and discussion

On-surface synthesis of [4]- and [5]-rhombenes

Our synthetic strategy toward [*n*]-rhombenes involves the design of the molecular precursors 7,14-bis(2,6-dimethylphenyl)ovalene (**3**) and 6,13-bis{10-(2,6-dimethylphenyl)anthracen-9-yl}-1,4,8,11-tetramethylpentacene (**4**) (Fig. 1), which are expected to undergo surface-catalyzed cyclodehydrogenation and oxidative cyclization of methyl groups, thereby yielding **1** and **2**, respectively. The synthesis of **3** (Fig. 1a) was performed starting from bisanthrone (**5**), which was treated with 2,6-dimethylphenylmagnesium bromide followed by dehydroxylation under an acidic condition to provide 10,10'-bis(2,6-dimethylphenyl)-9,9'-bianthracene (**6**). The oxidative cyclodehydrogenation of **6** gave 7,14-bis(2,6-dimethylphenyl)bisanthene (**7**), which was subjected to two-fold Diels-Alder addition with nitroethylene to obtain **3**. The synthesis of **4** (Fig. 1b) was performed through the Suzuki coupling of 9-bromoanthracene (**8**) with (2,6-dimethylphenyl)boronic acid to afford 9-(2,6-dimethylphenyl)anthracene (**9**), followed by its bromination to yield 9-bromo-10-(2,6-dimethylphenyl)anthracene (**10**). Subsequently, **10** was lithiated to {10-(2,6-dimethylphenyl)anthracen-9-yl}lithium and reacted with 1,4,8,11-tetramethylpentacene-6,13-dione to provide **4** after reduction. Toward the synthesis of **1**, **3** was deposited on a Au(111) surface, which was subsequently annealed to 300 °C to promote the on-surface reactions. High-resolution STM imaging elucidated that 92% of the molecules on the surface exhibit a uniform rhombic shape (Fig. 2a,b), and chemical structure determination via ultrahigh-resolution STM imaging^{34,35} unambiguously proved the formation of **1** (Fig. 2c). We further attempted the on-surface synthesis of **2** from **4** using a similar strategy. The overview STM image after annealing **4** at 300 °C on Au(111) revealed the predominance of covalently coupled molecular clusters (Fig. 2d and Supplementary Fig. 1), and in contrast to **1**, we rarely found isolated molecules on the surface. Figure 2e,f show the high-resolution and ultrahigh-resolution STM images of an isolated molecule, respectively, demonstrating the successful formation of **2**. The pronounced intermolecular reactions of **2** is indicative of a considerably higher reactivity of **2** compared to **1**, as the propensity for **1** under identical synthetic conditions is to remain isolated on the surface. As we demonstrate below, this drastic difference in the reactivity of **1** and **2** is due to a larger zigzag periphery in **2**, leading to an open-shell ground state.

To circumvent the problem of the limited yield of **2** on Au(111), we conducted the synthesis of **2** on Cu(110) surface. In contrast to densely-packed (111) surfaces, which exhibit weak interactions with molecular adsorbates, the more open (110) surfaces feature comparatively stronger hybridization between molecular orbitals and the metal *d*-states due to energetic upshift of the *d*-band center³⁶. As a result, molecular mobility may be substantially reduced³⁷ which could prevent intermolecular reactions and increase the yield of isolated molecules. Figure 2g presents an overview STM image after deposition of **4** on Cu(110) and

annealing to 240 °C. In contrast to Au(111), the reaction products on Cu(110) nearly exclusively consist of isolated molecules exhibiting a rhombic shape. The excellent match between the experimental STM image of the molecules (Fig. 2h) and the density functional theory (DFT)-simulated STM image of **2** on Cu(110) (Fig. 2i) proves the successful formation of **2**.

Tunneling spectroscopy measurements and theoretical calculations

We employ STS to experimentally probe the electronic structures of **1** and **2** on Au(111). Differential conductance spectroscopy (dI/dV , where I and V denote tunneling current and bias voltage, respectively) on **1** reveals peaks in the local density of states (LDOS) at -330 mV and $+400$ mV (Fig. 3a). Spatially resolved dI/dV maps at the respective energies exhibit excellent agreement with the DFT-LDOS maps of the HOMO and LUMO of **1** on Au(111) (Fig. 3b and Supplementary Fig. 2), confirming the spectroscopic features to be molecular orbital resonances, with the HOMO-LUMO gap being 730 meV. In contrast, dI/dV spectroscopy on **2** reproducibly reveals abrupt stepwise change in conductance symmetric around the Fermi energy, indicative of an inelastic excitation³⁸ (Fig. 3c and Supplementary Fig. 3). The excitation threshold, extracted from a fit to the corresponding IETS spectrum³⁹, equals ± 102 meV (Fig. 3d).

To investigate if the inelastic excitation may be ascribed to a spin excitation³³, we performed DFT calculations to unravel the magnetic ground states of $[n]$ -rhombenes. Since $[n]$ -rhombenes have an equal number of carbon atoms in the two interpenetrating triangular sublattices of their honeycomb lattice, the ground state, as per Lieb’s theorem for bipartite lattices^{40,41}, is expected to be a singlet, that is, the total spin quantum number $S = 0$. However, this rule does not predict whether a system with $S = 0$ ground state is an open-shell or a closed-shell singlet. Here, this complementary information is obtained from spin-polarized DFT calculations. Figure 4a presents the DFT energy difference between the open-shell singlet and closed-shell states for a series of $[n]$ -rhombenes in the gas phase, showing a size-dependent onset of magnetism. While for $n \leq 4$, the ground state is closed-shell, an open-shell singlet ground state emerges for $n \geq 5$, in agreement with previous reports^{4,42,43} and in support of our experimental observations. In particular, for **2**, the open-shell triplet ($S = 1$) and closed-shell states are 100 meV and 122 meV higher in energy, respectively, compared to the open-shell singlet ground state.

Furthermore, we calculated the magnetic excitation spectrum of **2** in the gas phase via an exact diagonalization of the Hubbard model at half filling^{44,45}—known to give results in agreement with advanced quantum chemistry methods³⁷—in the complete active space approximation with two electrons and two orbitals, with third nearest neighbor hopping. Figure 4b presents the energies of the manifold of excited states of **2** relative to its singlet ground state, as a function of the on-site Coulomb repulsion U . The first excited state is an open-shell triplet, with the corresponding singlet-triplet gap in the range of 75–150 meV for $t_1 \leq U \leq$

$2.5t_1$ (where $t_1 = 2.7$ eV is the nearest neighbor hopping parameter), in close correspondence to the experimental excitation threshold of 102 meV. Figure 4c presents the gas phase mean-field Hubbard spin polarization plot of **2**, where spin up and spin down populations are sublattice-polarized and localized at the opposite ends of the molecule. Therefore, while $S = 0$, a local spin polarization is maintained at each end. The corresponding picture in the case of a closed-shell ground state would entail equal population of spin up and spin down electrons at every carbon atom of **2**. Supplementary Fig. 4 shows the evolution of the frontier orbital gap, and the evolution of the total magnetic moment with U , for $[n]$ -rhombenes with $n = 2-7$.

Finally, to establish a quantitative link between the open-shell character of **2** on Au(111) to experimental measures of electronic structure (that is, orbital resonances), we performed many-body perturbation theory GW calculations⁴⁶ (where G and W denote Green's function and screened Coulomb potential, respectively), including screening effects from the underlying surface⁴⁷ (that is, GW+IC, where IC denotes image charge). Figure 4d presents a comparative energy spectrum of the HOMO-2 to LUMO+2 resonances of **2** determined from STS (Supplementary Figs. 5 and 6) and GW+IC calculations for the open-shell singlet and closed-shell states of **2**. Both the Coulomb gap and the relative energies of the HOMO-2 to LUMO+2 resonances obtained from GW+IC calculation for the open-shell singlet state of **2** (Coulomb gap: 800 meV) agree well with the corresponding experimental values (frontier gap: 900 meV), while the HOMO-LUMO gap of 320 meV from GW+IC calculation for the closed-shell state of **2** considerably differs from the experimental frontier gap, which thus provides a striking confirmation of the open-shell singlet ground state of **2** on Au(111). GW+IC calculation was also performed for the closed-shell state of **1**, where we also find a reasonable agreement of the theoretical HOMO-LUMO gap and relative energies of the HOMO-1 to LUMO+1 resonances with the corresponding experimental values (Supplementary Fig. 7), which confirms the closed-shell ground state of **1** on Au(111). We also conducted dI/dV spectroscopy of **2** on Ag(111) to probe any change in the MEC (Supplementary Fig. 8), where we detect a charge transfer from Ag(111) to **2**, leading to complete filling of the SOMOs and therefore a closed-shell ground state of **2**. In accordance with this observation, no spin excitations are seen for **2** on Ag(111). Finally, a short note regarding the influence of the surface on the electronic structure of the ZNGs reported in our work is apt. First, charge transfer between a molecule and surface can change the occupation of molecular orbitals that may quench magnetism⁴⁸. In addition, chemisorption has been shown to lead to notable bond-order reorganization in molecules⁴⁹, which may strongly influence their magnetic ground state. However, for both **1** and **2** on Au(111), charge transfer clearly does not take place since the frontier molecular orbitals of **1** (HOMO/LUMO) and **2** (SOMOs/SUMOs) are located far from the Fermi energy, and moreover, **1** and **2** are physisorbed on the surface (Supplementary Fig. 9). Second, the surface will also influence the magnetic excitation spectrum^{16,50} of **2** both via dynamical renormalization of the excitation energy due to Kondo exchange⁵¹, and screening of U and the hopping parameters^{52,53}.

Conclusion

For robust spin-logic operations at practical temperatures, it is imperative that the MEC exceeds the Landauer limit of minimum energy dissipation⁵⁴ at room temperature^{55,56}, $k_B T \ln(2) \approx 18$ meV, where k_B is the Boltzmann's constant and T is the temperature. The weak MEC of few millielectronvolts commonly found in transition metal nanomagnets limits the operation of devices based on such materials to cryogenic temperatures. In recent years, this issue has been partially addressed through the synthesis of magnetic nanographenes where the MEC is either close to the Landauer limit, as in chiral graphene nanoribbon junctions¹⁵ (up to 10 meV) and triangulene dimers¹⁹ (up to 14 meV), or slightly exceeds this limit, as in Clar's goblet¹⁶ (23 meV). In comparison, the experimental singlet-triplet gap of 102 meV of **2**, which provides a direct measure of the MEC, is more than five times larger than the Landauer limit—highly promising for room temperature stable spintronics. On a fundamental note, our results demonstrate that the synthesis of ZNGs with controlled size and shape allows building nanostructures with robust all-carbon magnetism, which constitute elementary building blocks to explore quantum magnetism. Given the robust MEC and negligible magnetic anisotropy in $[n]$ -rhombenes, construction of their nanoscale lattices through established on-surface synthetic techniques could pave the way for exploration of exotic low-dimensional quantum phases of matter^{57,58} in purely organic systems.

References

1. Yazyev, O. V. Emergence of magnetism in graphene materials and nanostructures. *Rep. Prog. Phys.* **73**, 056501 (2010).
2. Liu, S. & Langenaeker, W. Hund's multiplicity rule: a unified interpretation. *Theor. Chem. Acc.* **110**, 338–344 (2003).
3. Gryn'ova, G., Coote, M. L. & Corminboeuf, C. Theory and practice of uncommon molecular electronic configurations. *Wiley Interdiscip. Rev. Comput. Mol. Sci.* **5**, 440–459 (2015).
4. Yeh, C.-N. & Chai, J.-D. Role of Kekulé and Non-Kekulé Structures in the Radical Character of Alternant Polycyclic Aromatic Hydrocarbons: A TAO-DFT Study. *Sci. Rep.* **6**, 30562 (2016).
5. Das, A., Müller, T., Plasser, F. & Lischka, H. Polyradical Character of Triangular Non-Kekulé Structures, Zethrenes, p-Quinodimethane-Linked Bisphenalenyl, and the Clar Goblet in Comparison: An Extended Multireference Study. *J. Phys. Chem. A* **120**, 1625–1636 (2016).
6. Nakada, K., Fujita, M., Dresselhaus, G. & Dresselhaus, M. S. Edge state in graphene ribbons: Nanometer size effect and edge shape dependence. *Phys. Rev. B* **54**, 17954–17961 (1996).

7. Fernández-Rossier, J. & Palacios, J. J. Magnetism in Graphene Nanoislands. *Phys. Rev. Lett.* **99**, 177204 (2007).
8. Ezawa, M. Metallic graphene nanodisks: Electronic and magnetic properties. *Phys. Rev. B* **76**, 245415 (2007).
9. Konishi, A. et al. Synthesis and Characterization of Teranthene: A Singlet Biradical Polycyclic Aromatic Hydrocarbon Having Kekulé Structures. *J. Am. Chem. Soc.* **132**, 11021–11023 (2010).
10. Konishi, A. et al. Synthesis and Characterization of Quarteranthene: Elucidating the Characteristics of the Edge State of Graphene Nanoribbons at the Molecular Level. *J. Am. Chem. Soc.* **135**, 1430–1437 (2013).
11. Wang, S. et al. Giant edge state splitting at atomically precise graphene zigzag edges. *Nat. Commun.* **7**, 11507 (2016).
12. Huang, R. et al. Higher Order π -Conjugated Polycyclic Hydrocarbons with Open-Shell Singlet Ground State: Nonazethrene versus Nonacene. *J. Am. Chem. Soc.* **138**, 10323–10330 (2016).
13. Zeng, W. et al. Superoctazethrene: An Open-Shell Graphene-like Molecule Possessing Large Diradical Character but Still with Reasonable Stability. *J. Am. Chem. Soc.* **140**, 14054–14058 (2018).
14. Mishra, S. et al. On-surface synthesis of super-heptazethrene. *Chem. Commun.* **56**, 7467–7470 (2020).
15. Li, J. et al. Single spin localization and manipulation in graphene open-shell nanostructures. *Nat. Commun.* **10**, 200 (2019).
16. Mishra, S. et al. Topological frustration induces unconventional magnetism in a nanographene. *Nat. Nanotechnol.* **15**, 22–28 (2020).
17. Mishra, S. et al. Topological Defect-Induced Magnetism in a Nanographene. *J. Am. Chem. Soc.* **142**, 1147–1152 (2020).
18. Li, J. et al. Uncovering the Triplet Ground State of Triangular Graphene Nanoflakes Engineered with Atomic Precision on a Metal Surface. *Phys. Rev. Lett.* **124**, 177201 (2020).
19. Mishra, S. et al. Collective All-Carbon Magnetism in Triangulene Dimers. *Angew. Chem. Int. Ed.* **59**, 12041–12047 (2020).
20. Ajayakumar, M. R. et al. Toward Full Zigzag-Edged Nanographenes: peri-Tetracene and Its Corresponding Circumanthracene. *J. Am. Chem. Soc.* **140**, 6240–6244 (2018).
21. Mishra, S. et al. Tailoring Bond Topologies in Open-Shell Graphene Nanostructures. *ACS Nano* **12**, 11917–11927 (2018).

22. Rogers, C. et al. Closing the Nanographene Gap: Surface-Assisted Synthesis of Peripentacene from 6,6'-Bipentacene Precursors. *Angew. Chem. Int. Ed.* **54**, 15143–15146 (2015).
23. Morita, Y., Suzuki, S., Sato, K. & Takui, T. Synthetic organic spin chemistry for structurally well-defined open-shell graphene fragments. *Nat. Chem.* **3**, 197–204 (2011).
24. Goto, K. et al. A Stable Neutral Hydrocarbon Radical: Synthesis, Crystal Structure, and Physical Properties of 2,5,8-Tri-*tert*-butyl-phenalenyl. *J. Am. Chem. Soc.* **121**, 1619–1620 (1999).
25. Inoue, J. et al. The First Detection of a Clar's Hydrocarbon, 2,6,10-Tri-*tert*-Butyltriangulene: A Ground-State Triplet of Non-Kekulé Polynuclear Benzenoid Hydrocarbon. *J. Am. Chem. Soc.* **123**, 12702–12703 (2001).
26. Pavliček, N. et al. Synthesis and characterization of triangulene. *Nat. Nanotechnol.* **12**, 308–311 (2017).
27. Mishra, S. et al. Synthesis and Characterization of π -Extended Triangulene. *J. Am. Chem. Soc.* **141**, 10621–10625 (2019).
28. Su, J. et al. Atomically precise bottom-up synthesis of π -extended [5]triangulene. *Sci. Adv.* **5**, eaav7717 (2019).
29. Broene, R. D. & Diederich, F. The synthesis of circumanthracene. *Tetrahedron Lett.* **32**, 5227–5230 (1991).
30. Gu, Y., Wu, X., Gopalakrishna, T. Y., Phan, H. & Wu, J. Graphene-like Molecules with Four Zigzag Edges. *Angew. Chem. Int. Ed.* **57**, 6541–6545 (2018).
31. Gu, Y. et al. peri-Acenoacenes. *Chem. Commun.* **55**, 5567–5570 (2019).
32. Chen, Q., Schollmeyer, D., Müllen, K. & Narita, A. Synthesis of Circumpyrene by Alkyne Benzannulation of Brominated Dibenzo[*hi,st*]ovalene. *J. Am. Chem. Soc.* **141**, 19994–19999 (2019).
33. Hirjibehedin, C. F., Lutz, C. P. & Heinrich, A. J. Spin Coupling in Engineered Atomic Structures. *Science* **312**, 1021–1024 (2006).
34. Gross, L., Mohn, F., Moll, N., Liljeroth, P. & Meyer, G. The Chemical Structure of a Molecule Resolved by Atomic Force Microscopy. *Science* **325**, 1110–1114 (2009).
35. Kichin, G., Weiss, C., Wagner, C., Tautz, F. S. & Temirov, R. Single Molecule and Single Atom Sensors for Atomic Resolution Imaging of Chemically Complex Surfaces. *J. Am. Chem. Soc.* **133**, 16847–16851 (2011).
36. Peljhan, S. & Kokalj, A. DFT study of gas-phase adsorption of benzotriazole on Cu(111), Cu(100), Cu(110), and low coordinated defects thereon. *Phys. Chem. Chem. Phys.* **13**, 20408–20417 (2011).

37. Simonov, K. A. et al. From Graphene Nanoribbons on Cu(111) to Nanographene on Cu(110): Critical Role of Substrate Structure in the Bottom-Up Fabrication Strategy. *ACS Nano* **9**, 8997–9011 (2015).
38. Khanna, S. K. & Lambe, J. Inelastic Electron Tunneling Spectroscopy. *Science* **220**, 1345–1351 (1983).
39. Ternes, M. Spin excitations and correlations in scanning tunneling spectroscopy. *New J. Phys.* **17**, 063016 (2015).
40. Ovchinnikov, A. A. Multiplicity of the ground state of large alternant organic molecules with conjugated bonds. *Theoret. Chim. Acta* **47**, 297–304 (1978).
41. Lieb, E. H. Two theorems on the Hubbard model. *Phys. Rev. Lett.* **62**, 1201–1204 (1989).
42. Agapito, L. A., Kioussis, N. & Kaxiras, E. Electric-field control of magnetism in graphene quantum dots: Ab initio calculations. *Phys. Rev. B* **82**, 201411 (2010).
43. Ganguly, S., Kabir, M. & Saha-Dasgupta, T. Magnetic and electronic crossovers in graphene nanoflakes. *Phys. Rev. B* **95**, 174419 (2017).
44. Golor, M., Koop, C., Lang, T. C., Wessel, S. & Schmidt, M. J. Magnetic Correlations in Short and Narrow Graphene Armchair Nanoribbons. *Phys. Rev. Lett.* **111**, 085504 (2013).
45. Ortiz, R. et al. Exchange Rules for Diradical π -Conjugated Hydrocarbons. *Nano Lett.* **19**, 5991–5997 (2019).
46. Yang, L., Park, C.-H., Son, Y.-W., Cohen, M. L. & Louie, S. G. Quasiparticle Energies and Band Gaps in Graphene Nanoribbons. *Phys. Rev. Lett.* **99**, 186801 (2007).
47. Neaton, J. B., Hybertsen, M. S. & Louie, S. G. Renormalization of Molecular Electronic Levels at Metal-Molecule Interfaces. *Phys. Rev. Lett.* **97**, 216405 (2006).
48. van der Lit, J. et al. Suppression of electron–vibron coupling in graphene nanoribbons contacted via a single atom. *Nat. Commun.* **4**, 2023 (2013).
49. Majzik, Z. et al. Studying an antiaromatic polycyclic hydrocarbon adsorbed on different surfaces. *Nat. Commun.* **9**, 1198 (2018).
50. Schuler, B. et al. Reversible Bergman cyclization by atomic manipulation. *Nat. Chem.* **8**, 220–224 (2016).
51. Oberg, J. C. et al. Control of single-spin magnetic anisotropy by exchange coupling. *Nat. Nanotechnol.* **9**, 64–68 (2014).
52. Wehling, T. O. et al. Strength of Effective Coulomb Interactions in Graphene and Graphite. *Phys. Rev. Lett.* **106**, 236805 (2011).

53. Schüler, M., Rösner, M., Wehling, T. O., Lichtenstein, A. I. & Katsnelson, M. I. Optimal Hubbard Models for Materials with Nonlocal Coulomb Interactions: Graphene, Silicene, and Benzene. *Phys. Rev. Lett.* **111**, 036601 (2013).
54. Landauer, R. Irreversibility and Heat Generation in the Computing Process. *IBM J. Res. Dev.* **5**, 183–191 (1961).
55. Agarwal, H., Pramanik, S. & Bandyopadhyay, S. Single spin universal Boolean logic gate. *New J. Phys.* **10**, 015001 (2008).
56. Wang, W. L., Yazyev, O. V., Meng, S. & Kaxiras, E. Topological Frustration in Graphene Nanoflakes: Magnetic Order and Spin Logic Devices. *Phys. Rev. Lett.* **102**, 157201 (2009).
57. Savary, L. & Balents, L. Quantum spin liquids: a review. *Rep. Prog. Phys.* **80**, 016502 (2016).
58. Choi, D.-J. et al. Colloquium: Atomic spin chains on surfaces. *Rev. Mod. Phys.* **91**, 041001 (2019).

Acknowledgements

We thank D. Passerone for fruitful discussions, D. Schollmeyer for single crystal X-ray analysis and L. Rotach for technical support. This work was supported by the Swiss National Science Foundation (grant numbers 200020-182015 and IZLCZ2-170184), the NCCR MARVEL funded by the Swiss National Science Foundation (grant number 51NF40-182892), the European Union's Horizon 2020 research and innovation program (grant number 785219, Graphene Flagship Core 2), the Office of Naval Research (N00014-18-1-2708), the Max Planck Society, Ministry of Science and Innovation of Spain (grant numbers PID2019-106114GB-I00 and PID2019-109539GB), Generalitat Valenciana and Fondo Social Europeo (grant number ACIF/2018/175), MINECO-Spain (grant number MAT2016-78625), and Portuguese FCT (grant number UTAPEXPL/NTec/0046/2017). Computational support from the Swiss Supercomputing Center (CSCS) under project ID s904 is gratefully acknowledged.

Author Contributions

R.F., P.R., A.N. and K.M. conceived the project. Q.C. and X.Y. synthesized and characterized the precursor molecules. S.M. performed the STM experiments. S.M. analyzed the data with contributions from M.D.G. K.E. and C.A.P. performed the DFT and GW calculations. R.O., J.F.R., J.C.S.G., O.G. and S.M. performed the tight-binding and Hubbard calculations. All authors contributed to discussing the results and writing the manuscript.

Competing Interests

The authors declare no competing interests.

Figure 1 | Synthesis of [4]- and [5]-rhombenes. **a,b**, Combined in-solution and on-surface synthetic routes toward [4]- (**a**) and [5]-rhombene (**b**). Gray filled rings highlight Clar sextets. Conditions: (i) 2,6-dimethylphenylmagnesium bromide, THF, r.t., overnight; thereafter CH₃COOH, r.t., 10 min; (ii) NaI, NaH₂PO₂·H₂O, CH₃COOH, reflux, 2 h, 52% yield in two steps; (iii) DDQ, Sc(OTf)₃, CF₃SO₃H, chlorobenzene, 140 °C, 18 h, 25% yield; (iv) 2-nitroethanol, phthalic anhydride, *o*-xylene, 165 °C, 24 h, 68% yield; (v) 2,6-dimethylphenylboronic acid, Pd(OAc)₂, SPhos, K₃PO₄, toluene/H₂O, 120 °C, 18 h, 73% yield; (vi) Bromine, CCl₄, r.t., 15 min, 96% yield; (vii) *n*-BuLi, diethyl ether, -78 °C, 1 h, 1,4,8,11-tetramethylpentacene-6,13-dione, 0 °C, 48 h; (viii) NaI, NaH₂PO₂·H₂O, CH₃COOH, reflux, 6 h, 29% yield in two steps.

Figure 2 | On-surface synthesis and STM characterization of [4]- and [5]-rhombenes. **a**, Overview STM image after annealing **3** on Au(111) at 300 °C ($V = -300$ mV, $I = 120$ pA). **b,c**, High-resolution ($V = -330$ mV, $I = 50$ pA) (**b**) and Laplace-filtered ultrahigh-resolution ($V = -5$ mV, $I = 50$ pA, $\Delta = -0.8$ Å) (**c**) STM images of **1** on Au(111). a.u. denotes arbitrary units. **d**, Overview STM image after annealing **4** on Au(111) at 300 °C ($V = -400$ mV, $I = 100$ pA). Inset: High-resolution STM image of a cluster, where two constituent molecules corresponding to **2** are marked with arrows. **e,f**, High-resolution ($V = -10$ mV, $I = 50$ pA) (**e**) and Laplace-filtered ultrahigh-resolution ($V = -5$ mV, $I = 50$ pA, $\Delta = -0.9$ Å) (**f**) STM images of **2** on Au(111). **g**, Overview STM image after annealing **4** on Cu(110) at 240 °C ($V = -200$ mV, $I = 100$ pA). **h,i**, High-resolution ($V = -100$ mV, $I = 50$ pA) (**h**) and DFT-simulated ($V = -100$ mV) (**i**) STM images of **2** on Cu(110). Scale bars: 10 nm (**a,d,g**), 2 nm (inset **d**) and 0.5 nm (all other panels). Images in **b,c,e,f,h** were acquired with carbon monoxide (CO)-functionalized tips.

Figure 3 | Electronic and magnetic characterization of [4]- and [5]-rhombenes. **a**, dI/dV spectra acquired on **1** with a CO-functionalized tip revealing HOMO and LUMO resonances at -330 mV and +400 mV, respectively (open feedback parameters: $V = -600$ mV, $I = 200$ pA (left panel) and $V = +600$ mV, $I = 500$ pA (right panel); $V_{\text{rms}} = 16$ mV). All dI/dV spectra shown in individual panels are vertically offset for visual clarity. **b**, Constant-current dI/dV maps acquired with a CO-functionalized tip (upper panels) and corresponding DFT-LDOS maps (lower panels) at the HOMO and LUMO resonances of **1** on Au(111) ($V = -330$ mV, $I = 150$ pA; $V_{\text{rms}} = 20$ mV (HOMO dI/dV map) and $V = +380$ mV, $I = 160$ pA; $V_{\text{rms}} = 24$ mV (LUMO dI/dV map)). **c,d**, Background-subtracted dI/dV spectrum acquired on **2** with a CO-functionalized tip revealing inelastic excitation steps (open feedback parameters: $V = -200$ mV, $I = 200$ pA; $V_{\text{rms}} = 4$ mV) (**c**); and corresponding IETS spectrum (filled circles, open feedback parameters: $V = -200$ mV, $I = 2.8$ nA; $V_{\text{rms}} = 10$ mV), with fit to the experimental

data using the Heisenberg dimer model (solid line) (**d**). The spin excitation threshold is extracted to be ± 102 mV. Acquisition positions for the respective dI/dV spectra are marked with a blue filled circle in the inset ultrahigh-resolution STM images in **a,c**. The data in **c,d** were acquired on different molecules with different tips. Scale bar: 0.5 nm.

Figure 4 | Theoretical calculations. **a**, Gas phase DFT-computed energy difference between the open-shell singlet (OS) and closed-shell (CS) states of $[n]$ -rhombenes for $n = 2-7$. **b**, Gas phase excitation spectrum of **2** as a function of U (U is scaled with respect to t_1), obtained with an exact diagonalization of the Hubbard model. The energies are given with respect to the $S = 0$ singlet ground state (red curve). The first excited state corresponds to an open-shell triplet (blue curve). The dashed line indicates the experimental singlet-triplet gap of 102 meV obtained from IETS measurements. The two black curves correspond to $S = 0$ singlet states with strong Coulomb repulsion at large U due to double site occupancy. **c**, Gas phase mean-field Hubbard spin polarization plot of the open-shell singlet ground state of **2** calculated at $U = t_1$. Blue and red isosurfaces denote spin up and spin down populations. **d**, Energies of the HOMO-2 to LUMO+2 resonances of **2** on Au(111) from GW+IC calculations for the OS and CS states (orange and black markers, respectively), and STS measurements (purple markers). Filled circles indicate the corresponding frontier orbitals (HOMO/SOMOs and LUMO/SUMOs). Energies of the calculated and experimental levels are aligned at HOMO-2. The spin up and spin down GW+IC levels for the OS state are degenerate.

Methods

Synthesis of molecular precursors. The detailed solution synthesis of molecular precursors **3** and **4**, and associated characterization data are reported in Supplementary Figs. 10–32.

Sample preparation and STM/STS measurements. STM measurements were performed in a commercial low-temperature STM from Scienta Omicron operating at a temperature of 4.5 K and base pressure below 5×10^{-11} mbar. Au(111), Ag(111) and Cu(110) single crystal surfaces were prepared by Ar^+ sputtering and annealing cycles. Powder samples of precursors **3** and **4** were contained in quartz crucibles and sublimed from a home-built evaporator at 270 °C and 310 °C, respectively, onto single crystal surfaces held at room temperature. STM images and dI/dV maps were recorded in constant-current (that is, closed feedback loop) mode, and dI/dV and d^2I/dV^2 spectra were recorded in constant-height (that is, open feedback loop) mode. dI/dV and d^2I/dV^2 measurements were obtained with a lock-in amplifier operating at a frequency of 860 Hz. Modulation voltages for each measurement are reported as root mean squared amplitude (V_{rms}). Bias voltages are provided with respect to the sample. Unless otherwise noted, STM and STS measurements were performed with metallic tips. Ultrahigh-resolution STM images were acquired by scanning the molecules with CO-functionalized tips in constant-height mode, and the current channel is displayed. For ultrahigh-resolution STM

images, Δ indicates lowering of the tip height after opening the feedback loop at the center of the molecules. CO molecules were deposited on a cold sample (with a maximum sample temperature of 13 K) containing reaction products and post-deposited NaCl islands, which facilitate CO identification and pick up. The data reported in this study were processed with WaveMetrics Igor Pro or WSxM⁵⁹ software.

Tight-binding calculations. Tight-binding calculations have been performed by numerically solving the mean-field Hubbard Hamiltonian with third nearest neighbor hopping

$$\hat{H}_{MFH} = \sum_j \sum_{\langle\alpha,\beta\rangle_j,\sigma} -t_j c_{\alpha,\sigma}^\dagger c_{\beta,\sigma} + U \sum_{\alpha,\sigma} \langle n_{\alpha,\sigma} \rangle n_{\alpha,\bar{\sigma}} - U \sum_{\alpha} \langle n_{\alpha,\uparrow} \rangle \langle n_{\alpha,\downarrow} \rangle. \quad (1)$$

Here, $c_{\alpha,\sigma}^\dagger$ and $c_{\beta,\sigma}$ denote the spin selective ($\sigma \in \{\uparrow, \downarrow\}$ with $\bar{\sigma} \in \{\downarrow, \uparrow\}$) creation and annihilation operator at sites α and β , $\langle\alpha,\beta\rangle_j$ ($j = \{1, 2, 3\}$) denotes the nearest neighbor, second nearest neighbor and third nearest neighbor sites for $j = 1, 2$ and 3 , respectively, t_j denotes the corresponding hopping parameters (with $t_1 = 2.7$ eV, $t_2 = 0.1$ eV and $t_3 = 0.4$ eV for nearest neighbor, second nearest neighbor and third nearest neighbor hopping⁶⁰), U denotes the on-site Coulomb repulsion, $n_{\alpha,\sigma}$ denotes the number operator, and $\langle n_{\alpha,\sigma} \rangle$ denotes the mean occupation number at site α . Orbital electron densities, ρ , of the n^{th} -eigenstate with energy E_n have been simulated from the corresponding state vector $a_{n,i,\sigma}$ by

$$\rho_{n,\sigma}(\vec{r}) = \left| \sum_i a_{n,i,\sigma} \phi_{2p_z}(\vec{r} - \vec{r}_i) \right|^2, \quad (2)$$

where i denotes the atomic site index and ϕ_{2p_z} denotes the Slater $2p_z$ orbital for carbon.

The code provides tools to select the values for parameters, set up the geometry and the Hamiltonian, and solves it iteratively. Additionally, post-processing tools are provided to print and plot resulting quantities, such as energy levels, orbital maps and spin polarization.

The following Python code listing demonstrates how to select parameters, set up the Hamiltonian and solve it:

```
# import the main library and libraries for geometry import and plotting
import tb_mean_field_hubbard as tbmfh
import ase.io
import matplotlib.pyplot as plt

# Load the geometry using the ASE library
geometry = ase.io.read("5-rhombene.xyz")

# Set up the main object that facilitates all the calculations
mfh_model = tbmfh.MeanFieldHubbardModel(
    geometry,                # input geometry
    t_list = [2.7, 0.1, 0.4], # hoppings [1st, 2nd, 3rd] nearest-neighbor
    charge = 0,              # possibility to model ions
    multiplicity = 1         # determines the spin-state
```

```
)
# Solve the Hamiltonian for the specified Coulomb repulsion value
mfh_model.run_mfh(u = 3.0)
```

The following code listing demonstrates how to access the calculated properties and plot various post-processing analyses:

```
# access the resulting eigenvalues and eigenvectors
print(mfh_model.evals)
print(mfh_model.evecs)

# plot the eigenvector of the first orbital
mfh_model.plot_orbital(mo_index=0, spin=0)

# plot the LDOS mapping at a specific energy and height value
mfh_model.plot_sts_map(plt.gca(), energy=1.0, z=3.0)
```

Exact diagonalization of the Hubbard Hamiltonian. The exact diagonalization of the Hubbard Hamiltonian is carried out in the two-level system at half filling⁶¹, for which the energy levels $\pm U_M/2$ and $\pm\sqrt{4t_M^2 + U_M^2}/4$ of the system can be found analytically. The two levels, which are taken into consideration, are the sublattice-polarized zero energy states: $|1\rangle = 1/\sqrt{2}(|HOMO\rangle + |LUMO\rangle)$ and $|2\rangle = 1/\sqrt{2}(|HOMO\rangle - |LUMO\rangle)$, such that $t_M = \langle 1|\hat{H}|2\rangle$ and $U_M = U \sum_i |\langle i|1\rangle|^4$. Here, \hat{H} denotes the third nearest neighbor tight-binding Hamiltonian, U the on-site Coulomb repulsion of the carbon $2p_z$ orbital and $|i\rangle$ the $2p_z$ orbital of atomic site i .

DFT and GW calculations. The equilibrium geometries of the molecules adsorbed on Au(111) and Cu(110) surfaces were obtained with the CP2K code⁶² implementing DFT within a mixed Gaussian plane waves approach⁶³. The surface/adsorbate systems were modeled within the repeated slab scheme⁶⁴ in the following manner: for molecules on Au(111), the simulation cell contained 4 atomic layers of Au along the [111] direction and a layer of hydrogen atoms to passivate one side of the slab in order to suppress one of the two Au(111) surface states, and for molecules on Cu(110), the simulation cell contained 8 atomic layers of Cu along the [110] direction. 40 Å of vacuum was included in the simulation cell to decouple the system from its periodic replicas in the direction perpendicular to the surface. The electronic states were expanded with a TZV2P Gaussian basis set for C and H⁶⁵ and a DZVP basis set for Au and Cu. A cutoff of 600 Ry was used for the plane wave basis set. Norm-conserving Goedecker-Teter-Hutter pseudopotentials⁶⁶ were used to represent the frozen core electrons of the atoms. We used the PBE parameterization for the generalized gradient approximation of the exchange correlation functional⁶⁷. We used the D3 scheme proposed by Grimme et al. to account for van der Waals interactions⁶⁸. The Au surface was modeled by a supercell of 41.27×40.85 Å² corresponding to 224 surface units, and the Cu surface was modeled by a supercell of 43.20×35.65 Å² corresponding to 168 surface units. To obtain the equi-

librium geometries, we kept the atomic positions of the bottom two layers of the Au slab and the bottom four layers of the Cu slab fixed to the ideal bulk positions, and all other atoms were relaxed until forces were lower than 0.005 eV/Å. Simulated STM images^{69,70} within the Tersoff-Hamann approximation^{71,72} were obtained by extrapolating the electronic orbitals to the vacuum region in order to correct the wrong decay of charge density in vacuum due to the localized basis set⁷².

The gas phase geometry optimization and energy calculations for the restricted and unrestricted DFT were performed with the Martyna-Tuckerman Poisson solver together with a cell of size equal to double of the molecular bounding box plus 8 Å, while other inputs were kept equivalent to the slab calculation.

CP2K code was also used to perform the eigenvalue-self consistent GW calculations on the isolated molecular geometry corresponding to the adsorption conformation. The calculation was performed based on the unrestricted DFT-PBE wave functions. We employed the GTH pseudopotentials and analytic continuation with a two-pole model. The aug-DZVP basis set from Wilhelm et al. was used⁷³. To account for screening by the underlying metal surface, we applied the image charge model⁴⁷. To determine the image plane position with respect to the molecular geometry, we used a distance of 1.42 Å between the image plane and the first surface layer, as reported by Kharche and Meunier⁷⁴. The calculations were performed via workflows based on the AiiDA platform⁷⁵.

References

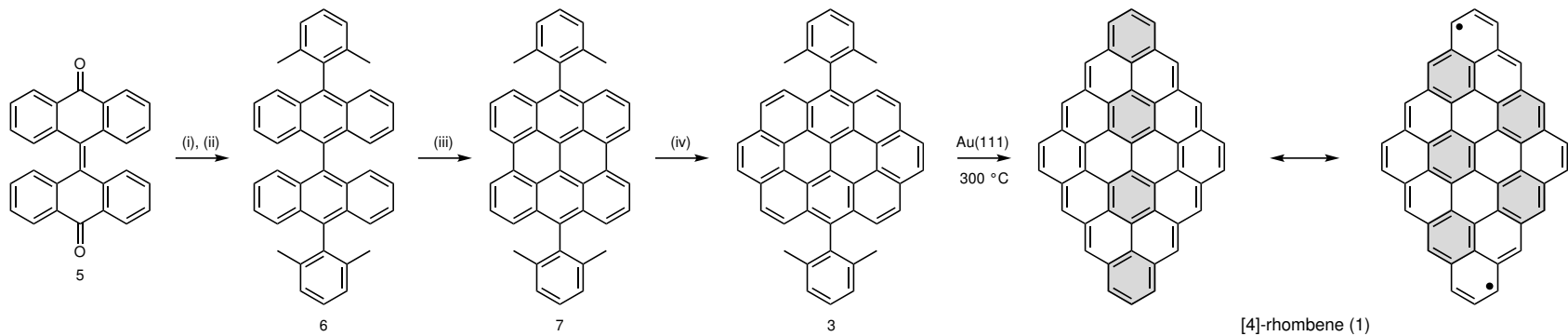
59. Horcas, I. et al. WSXM: A software for scanning probe microscopy and a tool for nanotechnology. *Rev. Sci. Instrum.* **78**, 013705 (2007).
60. Tran, V.-T., Saint-Martin, J., Dollfus, P. & Volz, S. Third nearest neighbor parameterized tight binding model for graphene nano-ribbons. *AIP Adv.* **7**, 075212 (2017).
61. Scalettar, R. T. An Introduction to the Hubbard Hamiltonian, lecture notes, Autumn School on Correlated Electrons: Quantum Materials: Experiments and Theory, Forschungszentrum Jülich (2016).
62. Hutter, J., Iannuzzi, M., Schiffmann, F. & VandeVondele, J. CP2K: atomistic simulations of condensed matter systems. *Wiley Interdiscip. Rev. Comput. Mol. Sci.* **4**, 15–25 (2014).
63. VandeVondele, J. et al. QUICKSTEP: Fast and accurate density functional calculations using a mixed Gaussian and plane waves approach. *Comput. Phys. Commun.* **167**, 103–128 (2005).
64. Pickett, W. E. Pseudopotential methods in condensed matter applications. *Comput. Phys. Rep.* **9**, 115–197 (1989).

65. VandeVondele, J. & Hutter, J. Gaussian basis sets for accurate calculations on molecular systems in gas and condensed phases. *J. Chem. Phys.* **127**, 114105 (2007).
66. Goedecker, S., Teter, M. & Hutter, J. Separable dual-space Gaussian pseudopotentials. *Phys. Rev. B* **54**, 1703–1710 (1996).
67. Perdew, J. P., Burke, K. & Ernzerhof, M. Generalized Gradient Approximation Made Simple. *Phys. Rev. Lett.* **77**, 3865 (1996).
68. Grimme, S., Antony, J., Ehrlich, S. & Krieg, H. A consistent and accurate ab initio parametrization of density functional dispersion correction (DFT-D) for the 94 elements H-Pu. *J. Chem. Phys.* **132**, 154104 (2010).
69. Gaspari, R. et al. *s*-orbital continuum model accounting for the tip shape in simulated scanning tunneling microscope images. *Phys. Rev. B* **84**, 125417 (2011).
70. Talirz, L. Toolkit using the Atomistic Simulation Environment (ASE). Available at: <https://github.com/ltalirz/asetk> (2015)..
71. Tersoff, J. D. & Hamann, D. R. Theory of the scanning tunneling microscope. *Phys. Rev. B* **31**, 805–813 (1985).
72. Tersoff, J. D. Method for the calculation of scanning tunneling microscope images and spectra. *Phys. Rev. B* **40**, 11990–11993 (1989).
73. Wilhelm, J., Del Ben, M. & Hutter, J. GW in the Gaussian and Plane Waves Scheme with Application to Linear Acenes. *J. Chem. Theory Comput.* **12**, 3623–3635 (2016).
74. Kharche, N. & Meunier, V. Width and Crystal Orientation Dependent Band Gap Renormalization in Substrate-Supported Graphene Nanoribbons. *J. Phys. Chem. Lett.* **7**, 1526–1533 (2016).
75. Pizzi, G., Cepellotti, A., Sabatini, R., Marzari, N. & Kozinsky, B. AiiDA: automated interactive infrastructure and database for computational science. *Comput. Mater. Sci.* **111**, 218–230 (2016).

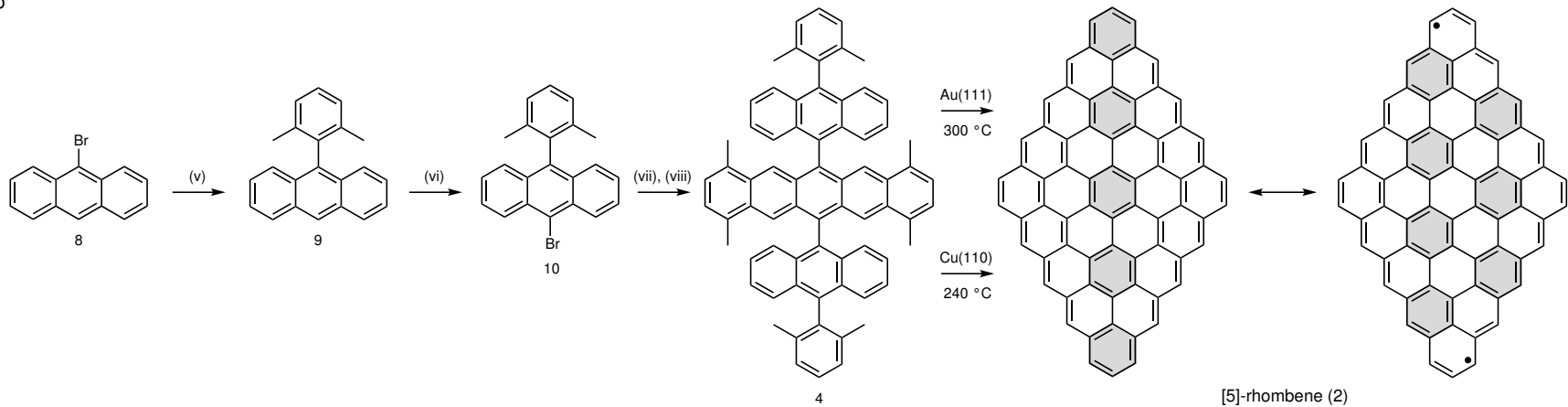
Data availability. Additional STM/STS data and theoretical calculations, materials and methods, solution synthetic procedures, and characterization data of chemical compounds (X-ray diffraction, NMR spectroscopy and high-resolution mass spectrometry) are available in the Supplementary Information. Crystallographic data for the structures reported in this Article have been deposited at the Cambridge Crystallographic Data Centre, under deposition numbers CCDC 1978171 (**3**) and 1978172 (**4**). Copies of the data can be obtained free of charge via <https://www.ccdc.cam.ac.uk/structures/>. Source data for Fig. 4 and Supplementary Figs. 4 and 7 are provided.

Code availability. The tight-binding calculations were performed using a custom-made Python program available on the GitHub repository (<https://github.com/eimrek/tb-mean-field-hubbard>).

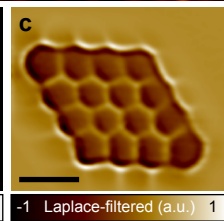
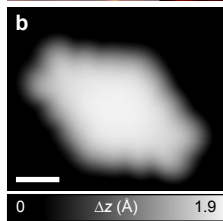
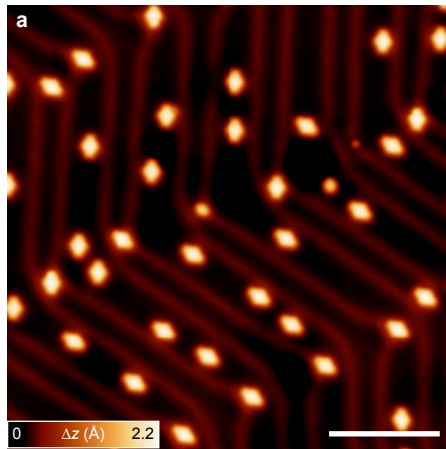
a



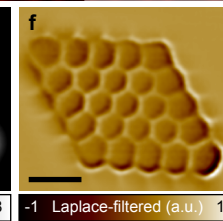
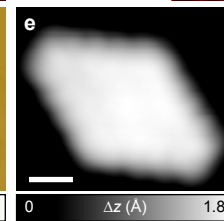
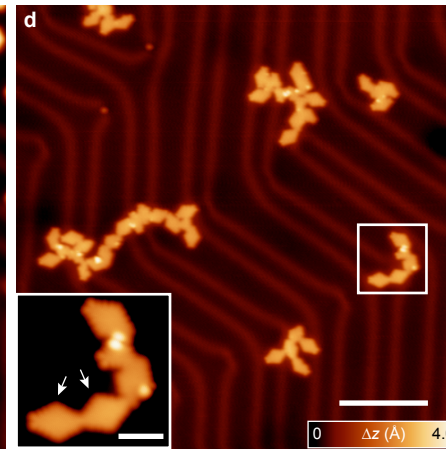
b



[4]-rhombene (1) on Au(111)



[5]-rhombene (2) on Au(111)



[5]-rhombene (2) on Cu(110)

